CrossMark

JFM RAPIDS
journals.cambridge.org/rapids

Heteroclinic path to spatially localized chaos in pipe flow

N. B. Budanur[1,2,†] **and B. Hof**[1]

[1]IST Austria, Am Campus 1, 3400 Klosterneuburg, Austria

[2]Kavli Institute for Theoretical Physics, UC Santa Barbara, Santa Barbara, CA 93106, USA

In shear flows at transitional Reynolds numbers, localized patches of turbulence, known as puffs, coexist with the laminar flow. Recently, Avila *et al.* (*Phys. Rev. Lett.*, vol. 110, 2013, 224502) discovered two spatially localized relative periodic solutions for pipe flow, which appeared in a saddle-node bifurcation at low Reynolds number. Combining slicing methods for continuous symmetry reduction with Poincaré sections for the first time in a shear flow setting, we compute and visualize the unstable manifold of the lower-branch solution and show that it extends towards the neighbourhood of the upper-branch solution. Surprisingly, this connection even persists far above the bifurcation point and appears to mediate the first stage of the puff generation: amplification of streamwise localized fluctuations. When the state-space trajectories on the unstable manifold reach the vicinity of the upper branch, corresponding fluctuations expand in space and eventually take the usual shape of a puff.

1. Introduction

In pipe flow, turbulence first appears in localized regions known as puffs. Puffs propagate downstream and eventually decay back to the laminar state or split to give birth to a new puff. Numerical and laboratory experiments in pipe flow (Avila *et al.* 2011) have shown that transition to sustained turbulence in a circular pipe happens when the rate of puff splitting exceeds that of decaying. Further research (Lemoult *et al.* 2016) has established that the dynamics and interplay of such localized turbulent domains give rise to a non-equilibrium phase transition. Instead of this stochastic point of view, we here apply the complementary deterministic dynamical systems approach in order to unravel details of puff formation.

The time evolution of a fluid flow can be thought of as a trajectory in an infinite-dimensional space. In this state space, a state of the fluid is a point, and

† Email address for correspondence: burak.budanur@ist.ac.at

its motion follows a one-dimensional curve. While Hopf (1948) articulated this dynamical viewpoint of turbulence, it has only recently been computationally feasible to tackle turbulence from this perspective. From this geometrical viewpoint, the state space of a transitional shear flow contains a linearly stable equilibrium, laminar flow and a chaotic saddle, turbulence, which for the parameter regime considered here is of transient nature.

The state-space geometry of a chaotic system is shaped by time-invariant solutions, such as equilibria and periodic orbits, and their stable/unstable manifolds (Cvitanović *et al.* 2015). Such invariant solutions that are embedded in chaotic sets are unstable; hence they are visited by the flow only transiently. Flow approaches an invariant solution following its stable manifold and leaves its neighbourhood on its unstable manifold. This intuition suggests the search for invariant solutions as the first step of the turbulence problem from Hopf's perspective.

Over the past three decades, many nonlinear equilibrium and periodic solutions have been found computationally for canonical shear flows at transitional Reynolds numbers (*Re*) (see Kawahara, Uhlmann & van Veen (2012) for a review), and flow structures similar to some of the solutions found numerically have been observed in experiments for the case of pipe flow (Hof *et al.* 2004). A general feature of these solutions is that they appear as pairs in saddle-node bifurcations at low *Re* or through further bifurcations of such saddle-node pairs. Moreover, the lower-energy ones of these solutions appeared to belong to a state-space region between laminar and turbulent dynamics. Itano & Toh (2001) used this property to find their travelling wave solution in plane Poiseuille flow. They employed a shooting method that bisects between initial conditions that laminarize and those that develop into turbulence, and found a travelling wave whose stable manifold sets the basin boundary of turbulence. Kawahara & Kida (2001) adapted this method to plane Couette flow and discovered a previously unknown periodic orbit. In pipe flow, a similar search yielded a seemingly chaotic state, albeit with dynamics simpler than those of the turbulence (Schneider, Eckhardt & Yorke 2007). Later on, Duguet, Willis & Kerswell (2008) showed numerical evidence that this state is organized in the vicinity of a travelling wave initially found by Pringle & Kerswell (2007), and approaches to this solution were observed in pipe flow experiments by de Lozar *et al.* (2012).

Most of the early studies of invariant solutions in shear flows were restricted to small computational domains called minimal flow units (Jiménez & Moin 1991) that are only large enough to capture essential statistics of turbulence. However, such small domains cannot capture streamwise localization of turbulent spots, which are relevant to the onset of turbulence. Avila *et al.* (2013) numerically studied the laminar–turbulent boundary in a 40-diameter-long periodic pipe, a domain large enough to exhibit localization. They discovered that when the flow is restricted to the invariant subspace of solutions that have two-fold rotational and reflectional symmetries in azimuth, the laminar–turbulent boundary is set by the stable manifold of a single relative periodic orbit, that is a periodic orbit with a spatial shift. By numerical continuation they showed that this solution is the lower branch of a saddle-node pair, akin to invariant solutions found in small domains.

For a complete understanding of the state-space geometry, numerical identification of dynamically relevant invariant solutions must be followed by preparation of a catalogue of possible motions in their neighbourhood. Recently, Suri *et al.* (2017) experimentally demonstrated that this approach can be used as a predictive tool on a weakly turbulent quasi-two-dimensional flow. For three-dimensional shear flows computation of unstable manifolds of invariant solutions is a technically

challenging task because they can be very high-dimensional. Moreover, the presence of continuous symmetries further complicates the problem since each continuous symmetry introduces a new marginal direction, increasing the dimension of the associated unstable manifold by one. The main technical contribution of the current work is to resolve this issue by combining the method of slices with Poincaré sections for computation and visualization of the unstable manifold of a relative periodic orbit. Applying this technique, we show for the aforementioned case of the localized lower-branch relative periodic orbit that its unstable manifold extends towards the neighbourhood of the corresponding upper-branch solution. Our results demonstrate that this state-space structure governs the first stage of puff formation, which corresponds to the amplification of localized disturbances in the physical space. Once the unstable manifold reaches the vicinity of the upper-branch solution, the disturbances begin to expand and take the typical shape of a puff.

The paper is organized as follows. In the next section, we describe the numerical procedure and introduce our notation. Technical aspects, the simple symmetry reduction scheme and the computation of unstable manifolds on a Poincaré section are presented in §§ 3 and 4. The results are discussed in § 5. The main text is supplemented by appendix A, where we derive projection operators, which we use in our computations.

2. Numerical set-up and notation

For numerical simulations, we use Openpipeflow (Willis 2017), which integrates the Navier–Stokes equations for fluctuations $\boldsymbol{u}$ around the base (Hagen–Poiseuille) solution. The axial pressure gradient is adjusted throughout the simulation in order to ensure a constant flux equal to that of the base flow at a given $Re = UD/\nu$, where U is the mean axial velocity, D is the pipe diameter and ν is the kinematic viscosity of the fluid. The flow field satisfies the incompressibility condition $\nabla \cdot \boldsymbol{u} = 0$ throughout the volume; there are periodic boundary conditions $\boldsymbol{u}(z, \theta, r) = \boldsymbol{u}(z + L, \theta, r)$ and $\boldsymbol{u}(z, \theta, r) = \boldsymbol{u}(z, \theta + 2\pi, r)$ in axial and azimuthal directions, and the no-slip boundary condition $\boldsymbol{u}(z, \theta, r = D/2) = 0$ on the pipe wall. For spatial discretization, flow fields are expanded in Fourier series in axial and azimuthal directions and finite differences are used to evaluate derivatives in the radial direction. In the numerical work presented here, the computational domain is $L = 25D$ long and Fourier series in axial and azimuthal directions are respectively truncated at $K = 192$ and $M = 16$, and $N = 64$ finite difference points are used in the radial direction. Nonlinear terms are evaluated following the 3/2-rule for dealiasing resulting in $64 \times 576 \times 48$ spatial grid points. We adopted our resolution from Chantry, Willis & Kerswell (2014), who studied bifurcations of the localized solutions considered here from travelling waves as the pipe length is increased. We checked our results for robustness at higher spatial resolution $(N, K, M) = (128, 320, 32)$. Re is set to 1700, at which puffs have long lifetimes (up to $1000\,D/U$) in the symmetry subspace considered here.

Pipe flow is equivariant under streamwise translations $g_z(l)\boldsymbol{u}(z, r, \theta) = \boldsymbol{u}(z - l, r, \theta)$, azimuthal rotations $g_\theta(\phi)\boldsymbol{u}(z, r, \theta) = \boldsymbol{u}(z, r, \theta - \phi)$ and the azimuthal reflection $\sigma[u, v, w](z, r, \theta) = [u, v, -w](z, r, -\theta)$, where u, v, w are velocity field components in the axial, radial and azimuthal directions respectively. Following Avila *et al.* (2013), we restrict our study to the velocity fields that are symmetric under rotation by π, $g_\theta(\pi)\boldsymbol{u} = \boldsymbol{u}$, and the reflection $\sigma\boldsymbol{u} = \boldsymbol{u}$. Imposing reflection invariance breaks the continuous rotation symmetry of the system, allowing only for half-domain rotations.

Since we are considering the subspace invariant under rotation by π, half-domain rotations are given by $g_\theta(\pi/2)$, hence the symmetry group of the system becomes $G = \{g_z(l), g_\theta(\pi/2)\}$.

For clarity, we are going to use state-space notation. Let $a(t)$ be a vector containing all $(3 \times 64 \times 384 \times 32)$ numerical degrees of freedom of the flow fields $[u, v, w]$. Evolution under Navier–Stokes equations implies a finite-time flow mapping $f^\tau(a(0)) = a(\tau)$ that takes a solution at time 0 to a new one at time τ. In this formalism, equivariance under $g \in G$ means that the flow and the symmetry operation commute, i.e. $gf^\tau(a(0)) = f^\tau(ga(0))$. Throughout this article, our notation will not distinguish between an abstract group element and its particular representation. Thus, whenever a group action is present, its appropriate representation on the corresponding velocity fields is implied. Finally, we need to introduce an inner product to use in our calculations. Our choice is the standard 'energy norm': let a and a' be state-space vectors corresponding to velocity fields $\boldsymbol{u}$ and $\boldsymbol{u}'$. We define the L_2 inner product as $\langle a, a' \rangle = (1/2) \int \boldsymbol{u} \cdot \boldsymbol{u}' \, \mathrm{d}V$; hence $\|a\|^2 = \langle a, a \rangle$ is the kinetic energy of a.

A relative periodic orbit is a recurrence (after the orbit's period T_p') up to a symmetry operation

$$f^{T_p'}(a_p) = g_p' a_p. \tag{2.1}$$

For the pair of relative periodic orbits found by Avila *et al.* (2013), $g_p' = g_\theta(\pi/2)g_z(l_p')$. For simplicity, we are going to treat this orbit as if its period were twice its fundamental period $T_p = 2T_p'$, and its only symmetry is a streamwise shift since $g_p = (g_p')^2 = g_z(l_p = 2l_p')$.

A relative periodic orbit with a one-parameter compact continuous symmetry defines a 2-torus

$$\{g_z(l)f^\tau(a_p) \mid \tau \in [0, T_p), l \in [0, L)\} \tag{2.2}$$

in the state space, which is parametrized by shifts l and time τ. The stability of a relative periodic orbit is determined by the eigenvalues of the Jacobian matrix

$$\boldsymbol{J}_p = g_p^{-1} \, \mathrm{d}f^{T_p}(a_p)/\mathrm{d}a_p, \tag{2.3}$$

which are known as Floquet multipliers (Chossat & Lauterbach 2000; Cvitanović *et al.* 2015). Since this Jacobian matrix (2.3) is very large, in practice, we compute the leading Floquet multipliers Λ_i and the corresponding Floquet vectors V_i via Arnoldi iteration (Trefethen & Bau 1997). The lower-branch relative periodic orbit of Avila *et al.* (2013) has only one positive real Floquet multiplier Λ_1 greater than one, two marginal $\Lambda_{2,3} = 1$ multipliers corresponding to the disturbances as axial and temporal shifts; the rest $|\Lambda_{i>3}|$ of the multipliers have absolute values smaller than one. Counting axial and temporal shift directions, the unstable manifold of this relative periodic orbit is three-dimensional. However, these marginal directions are of no dynamical importance and our next step is to cancel them.

3. Reductions

For a $(1 + 1)$-dimensional partial differential equation under a periodic boundary condition, Budanur *et al.* (2015) show that the translational symmetry can be reduced by fixing the phase of the first Fourier mode to 0, and this transformation can be interpreted as a 'slice', that is a codimension-1 hyperplane where all symmetry-equivalent state-space points are represented by a single point. Extension of this method to the canonical shear flows requires a particular choice for the
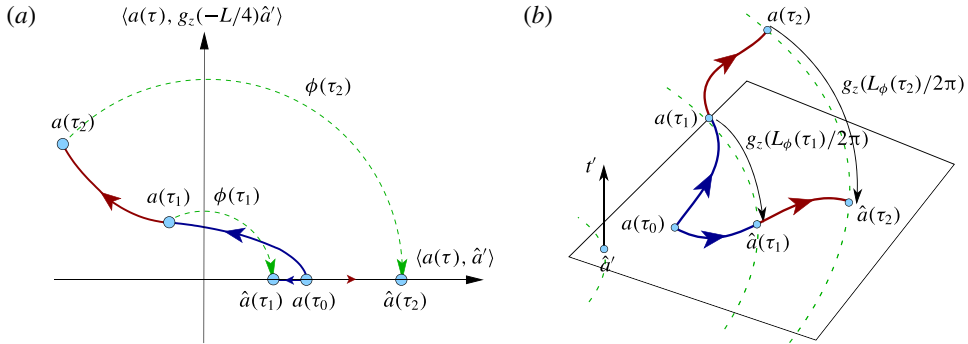
FIGURE 1. Sketches of two different formulations of continuous symmetry reduction by the first Fourier mode slice. (*a*) Projection of a full state-space trajectory $a(\tau)$ on a two-dimensional hyperplane spanned by $(\hat{a}', g_z(-L/4)\hat{a}')$. Symmetry-fixing phases $\phi(\tau)$ (3.3) are shown for instances τ_1 and τ_2. (*b*) Slice hyperplane defined by (3.4) and the transformation of full state-space trajectory $a(\tau)$ onto the slice by the action of $g_z(L\phi(\tau)/2\pi)$.

slice template's dependence on the non-homogeneous directions. Willis, Short & Cvitanović (2016) adapted this idea to the study of a short ($L \approx 1.85$) pipe with imposed shift-and-reflect symmetry: they experimentally selected a typical turbulent state for this purpose, retained its dependence on the radial and azimuthal coordinates, while imposing a $\cos(2\pi z/L)$ dependence in the axial direction. Here, we take a much simpler approach and define a first Fourier mode slice template $\hat{a}'$ as the state vector corresponding to the three-dimensional field

$$[\hat{u}', \hat{v}', \hat{w}'](z, \theta, r) = \mathrm{J}_0(\alpha r)\cos(2\pi z/L), \tag{3.1}$$

where J_0 is the zeroth Bessel function of the first kind and α is chosen such that $\mathrm{J}_0(\alpha D/2) = 0$. For a given trajectory $a(\tau)$, we can now define a symmetry-reduced trajectory as

$$\hat{a}(\tau) = g_z(L\phi/2\pi)a(\tau), \tag{3.2}$$

where

$$\phi(\tau) = \arg(\langle a(\tau), \hat{a}'\rangle + i\langle a(\tau), g_z(-L/4)\hat{a}'\rangle). \tag{3.3}$$

The pair of state-space vectors $\hat{a}', g_z(-L/4)\hat{a}'$ are orthogonal to each other and span a two-dimensional subspace. As depicted in figure 1(*a*), the slice-fixing phase ϕ in (3.3) is the polar angle when a state is projected onto this hyperplane. Transformation (3.2) fixes this angle to 0, defining a unique symmetry-reduced $\hat{a}(\tau)$ for all $a(\tau)$. We have chosen the r dependence of the slice template in (3.1) to be a Bessel function because of the cylindrical geometry. In practice, many other choices can be equally good for the purpose of symmetry reduction.

Our next step is to redefine the transformation (3.2) as a slice, a codimension-1 half-hyperplane

$$\langle \hat{a}(\tau) - \hat{a}', t'\rangle = 0, \quad \langle t(\hat{a}), t'\rangle > 0, \tag{3.4a,b}$$

where $t(\hat{a}) = T_z\hat{a}$ is the group tangent, $t' = t(\hat{a}')$ is the slice tangent, T_z is the generator of infinitesimal translations, satisfying $g_z(l) = \exp(T_z l)$. In our particular case, $T_z\mathbf{u} = -\mathrm{d}\mathbf{u}/\mathrm{d}z$, hence $t' = (2\pi/L)g_z(-L/4)\hat{a}'$. After defining the slice by (3.4), one looks for the phases ϕ such that $g_z(L\phi/2\pi)a(\tau)$ satisfies (3.4) as sketched in figure 1(*b*).

At first sight, redefining the polar coordinate transformation (3.2) as a slice (3.4) might seem an overcomplication; however, this reformulation provides some important tools. In particular, one can derive (see appendix A) the projection operator

$$\boldsymbol{H}(\hat{a}) = 1 - \frac{t(\hat{a}) \otimes t'}{\langle t(\hat{a}),\ t' \rangle} \qquad (3.5)$$

that projects infinitesimal perturbations to $\hat{a}$ from full state space to the slice. With (3.4) and (3.5), we can now reduce the torus (2.2) to a closed curve and define its stability. Let a_p be a point on a relative periodic orbit and V_i be the Floquet vectors computed at this point. If $\hat{a}_p = g(L\phi_p/2\pi)a_p$ is the symmetry-reduced state-space point corresponding to a_p, then the symmetry-reduced Floquet vectors are $\hat{V}_i = \boldsymbol{H}(\hat{a}_p)g(L\phi_p/2\pi)V_i$. Note that $\boldsymbol{H}(\hat{a})t(\hat{a}) = 0$, thus the continuous symmetry direction is eliminated in the slice.

It can be shown (Guckenheimer & Holmes 1983; Cvitanović *et al.* 2015) that in the vicinity of a periodic orbit of a dynamical system, one can define a Poincaré map, which contains a fixed point, whose stability multipliers are equal to the Floquet multipliers of the periodic orbit, except for the marginal multiplier corresponding to the time direction that is eliminated by the Poincaré section. Moreover, the stability eigenvectors in the Poincaré section can be obtained from Floquet vectors by a projection. We define such a Poincaré section as

$$\langle \hat{a}_{\mathcal{P}} - \hat{a}_p,\ \hat{v}(\hat{a}_p) \rangle = 0, \quad \langle \hat{v}(\hat{a}_{\mathcal{P}}),\ \hat{v}(\hat{a}_p) \rangle > 0, \qquad (3.6a,b)$$

where $\hat{v}(\hat{a}) = \boldsymbol{H}(\hat{a})v(\hat{a})$ and $v(a) = \lim_{\delta\tau \to 0}(f^{\delta\tau}(a) - a)/\delta\tau$ is the state-space velocity. Continuous-time symmetry-reduced flow $\hat{a}(\tau) = \hat{f}^\tau(\hat{a}(0))$ induces a discrete-time dynamical system $\hat{a}_{\mathcal{P}}[n] = \hat{f}_{\mathcal{P}}^n(\hat{a}_{\mathcal{P}}[0])$, where n counts the number of intersections of trajectories with the Poincaré section as the discrete-time variable. Finally, we define the operator that reduces the infinitesimal perturbations to $\hat{a}_{\mathcal{P}}$ from the symmetry-reduced state space to the Poincaré section as

$$\boldsymbol{P}(\hat{a}_{\mathcal{P}}) = 1 - \frac{\hat{v}(\hat{a}_{\mathcal{P}}) \otimes \hat{v}(\hat{a}_p)}{\langle \hat{v}(\hat{a}_{\mathcal{P}}),\ \hat{v}(\hat{a}_p) \rangle}, \qquad (3.7)$$

which allows us to project the symmetry-reduced Floquet vectors $\hat{V}_i$ onto the Poincaré section as $\hat{V}_{i,\mathcal{P}} = \boldsymbol{P}(\hat{a}_p)\hat{V}_i$. Similar to (3.5), the projection operator (3.7) follows from (A 6).

4. The unstable manifold

Budanur & Cvitanović (2017) demonstrate the approximation of one- and two-dimensional unstable manifolds of relative periodic orbits on Poincaré sections for the Kuramoto–Sivashinsky system. The main idea is to select trajectories that approximately cover the linear unstable manifold, hence their forward integration approximately covers the nonlinear unstable manifold; see Budanur & Cvitanović (2017) for details. Here, we are interested in computing the unstable manifold of the lower-branch relative periodic orbit (LB) of Avila *et al.* (2013) at $Re = 1700$. At this Re, the only unstable Floquet multiplier of LB is $\Lambda_1 = 2.8291523$. Initial conditions on the Poincaré section that approximately cover the associated unstable manifold are

$$\hat{a}_{\mathcal{P}}(\delta) = \hat{a}_{p,\mathcal{P}} \pm \epsilon \Lambda_1^\delta \hat{V}_{1,\mathcal{P}}, \qquad (4.1)$$
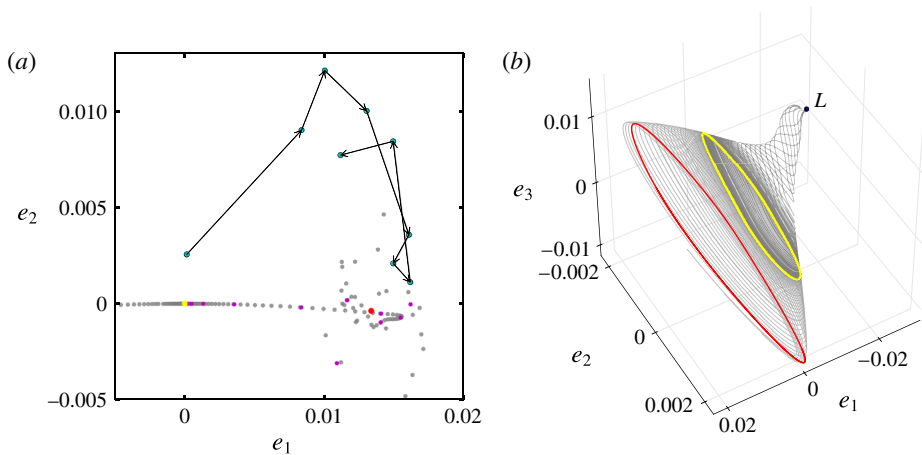
FIGURE 2. (*a*) Unstable manifold of LB (grey dots) and a small perturbation (cyan circles) to the laminar flow that develops into a puff on the Poincaré section (3.6). The direction of discrete time from $n = 0$ to $n = 9$ is indicated by arrows for the perturbation. Intersections of relative periodic orbits LB and UB with the Poincaré section are marked yellow and black respectively. Magenta markers correspond to the orbit with the initial condition $\hat{a}_{\mathcal{P}}(\delta = 0)$. Few points on the unstable manifold to the left of LB are shown because this direction consists of laminarizing orbits. (*b*) Three-dimensional projection of the trajectories (grey) that populate the unstable manifold of LB along with the LB (yellow) and UB (red) within the slice. The laminar equilibrium is annotated with *L*.

where $\delta \in [0, 1)$ and ϵ is a small constant. Note that under discrete-time linear dynamics, the first return of the initial condition $\hat{a}_{\mathcal{P}}(0)$ corresponds to $\hat{a}_{\mathcal{P}}(1)$; therefore, forward integrating these initial conditions populates the one-dimensional unstable manifold on the Poincaré section. Openpipeflow normalizes Floquet vectors such that their magnitudes are equal to that of the initial point on the relative periodic orbit, i.e. $\|V_i\| = \|a_p\|$. Projection onto the Poincaré section and setting $\epsilon = 10^{-4}$ yields the relative amplitude of the initial perturbation as $\epsilon \|\hat{V}_{1,\mathcal{P}}\| / \|\hat{a}_{p,\mathcal{P}}\| \approx 0.68 \times 10^{-4}$. In order to approximate the unstable manifold, we chose nine equidistant points in [0, 1) for δ and forward integrated these initial conditions while recording their intersections with the Poincaré section (3.6).

Figure 2 shows the unstable manifold approximated this way. In panel (*a*), we show the first 15 intersections of each trajectory with the Poincaré section, projected onto bases formed by the unstable Floquet vector $\hat{V}_1$ and the real part of the least stable Floquet vector $\hat{V}_4$ of LB, orthonormalized by the Gram–Schmidt procedure, namely $e_1 = \langle \hat{a}_{\mathcal{P}} - \hat{a}_p, \hat{V}_{1,\perp} \rangle$, $e_2 = \langle \hat{a}_{\mathcal{P}} - \hat{a}_p, \operatorname{Re}\hat{V}_{4,\perp} \rangle$, where subscript $\perp$ implies that vectors are orthonormalized. We observed that as the trajectories leave the neighbourhood of LB (the origin of figure 2) they approach the upper branch (UB). In figure 2(*b*) we visualize same trajectories as three-dimensional projections from the first Fourier mode slice along with LB and UB, where for the third projection direction we used the symmetry-reduced state-space velocity vector evaluated at $\hat{a}_p$, i.e. $e_3 = \langle \hat{a}(\tau) - \hat{a}_p, \hat{v}(\hat{a}_p)/\|\hat{v}(\hat{a}_p)\| \rangle$. Here, relative periodic orbits are closed periodic orbits as expected; and the unstable manifold appears two-dimensional. The manifold's approach to the UB is also clearly visible on this projection. Additionally, we are also able to visualize laminarizing part of the unstable manifold.
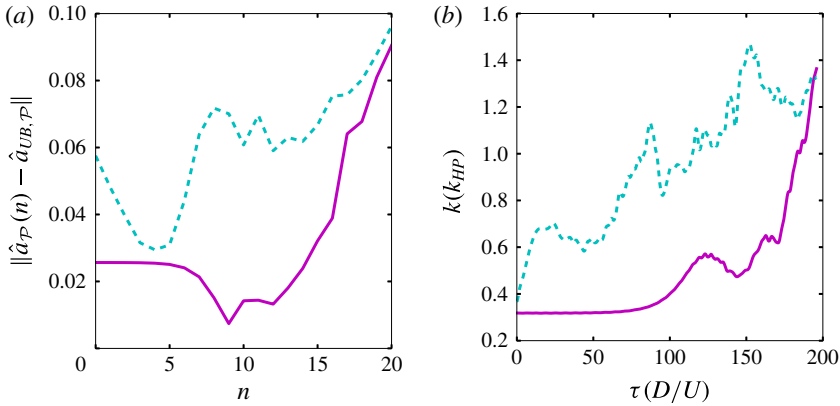
FIGURE 3. (*a*) L_2 distance from UB on the Poincaré section for 20 returns. (*b*) Time evolution of kinetic energy in units of the kinetic energy k_{HP} of the laminar flow. Magenta (solid): a trajectory on the unstable manifold of LB, cyan (dashed): puff transition initiated by a small perturbation to the laminar state.

Another trajectory shown in figure 2(*a*) is an initially small perturbation developing into a puff. We generated this perturbation by taking a typical puff state and scaling its amplitude by 0.5. Nine discrete-time steps displayed in Figure 2(*a*) show its approach to UB before redeveloping into a puff. We observed this behaviour in numerical experiments prepared with similar initial conditions. Of course, this is not extremely surprising: if we started with an initial condition that is only large enough for triggering turbulence, then the trajectory would have closely followed the unstable manifold of LB since the numerical evidence strongly suggests that the laminar–turbulent boundary is set by its stable manifold. Nevertheless, it is worth noting that the signatures of UB could be seen in puff formation without the need to prepare very precise initial conditions through a bisection procedure.

In order to confirm apparent approaches to the UB, we measured the trajectories' distance from it on the Poincaré section. Figure 3(*a*) shows the distance of the orbit with initial condition $\hat{a}_{\mathcal{P}}(\delta = 0)$ on the unstable manifold of LB (shown magenta in figure 2) and the perturbation we show in figure 2 from the UB. For both trajectories, we see a clear initial drop before they move away following the unstable manifold of the UB. For further comparison, we show the time evolution of turbulent kinetic energy for both trajectories in figure 3(*b*). Note for the trajectory on the unstable manifold that before the kinetic energy goes up to puff levels ($\sim 1.4k_{HP}$) it oscillates around $0.5k_{HP}$ during $\tau \in (125, 175)(D/U)$. Similarly, for the small perturbation, after an initial increase, the kinetic energy stays close to $0.6k_{HP}$ during $\tau \in (25, 75)(D/U)$ before further increasing to puff levels. Both episodes correspond to the approach of trajectories to UB. Note that the time interval shown in figure 3(*a*) is not necessarily the same for each orbit, nor are the discrete-time intervals equal to each other. For the perturbation, the interval $n \in [0, 20]$ corresponds to $\tau \in (0, 146.25)(D/U)$, whereas for the trajectory on the unstable manifold, it corresponds to $\tau \in (0, 193.67)(D/U)$.

For further comparison, we visualized streamwise velocity and vorticity isosurfaces for three snapshots ($n = 0, 9, 20$) on the orbit with initial condition $\hat{a}_{\mathcal{P}}(\delta = 0)$ (magenta on figure 2) respectively in figure 4(*a*,*c*,*f*). At the closest approach ($n = 9$, figure 4*c*) the resemblance of flow structures of the unstable manifold to those of UB (figure 4*e*) is very close. In addition, we show flow structures for two snapshots
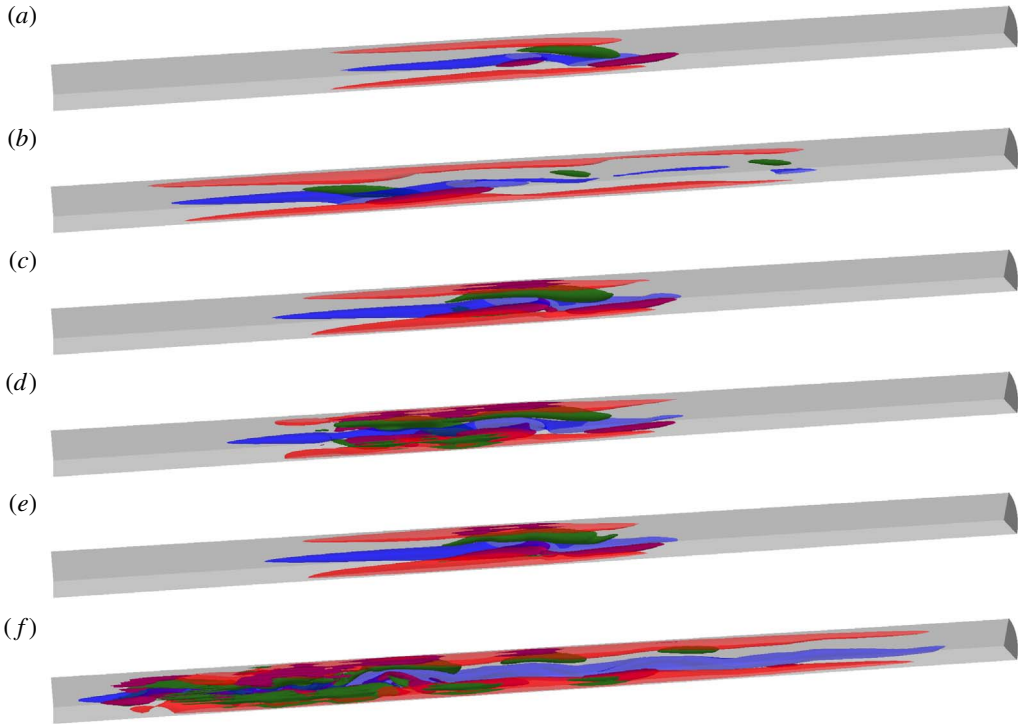
(*a*)

(*b*)

(*c*)

(*d*)

(*e*)

(*f*)

FIGURE 4. Isosurfaces of streamwise vorticity at $\omega_z = \pm 2.0\, U/D$ (purple and green) and streamwise velocity at $u = \pm 0.4\, U$ (red and blue) for the trajectory on LB's unstable manifold at $n = 0, 9, 20$ (*a,c,f*), for the small perturbation at $n = 0, 4$ (*b,d*) and for UB (*e*). Shown here is the pipe region $z \in [5, 20]D$, $\theta \in [0, \pi/2]$ since the rest of the structures can be obtained from reflection and rotation by π symmetries that are present.

of the orbit shown with cyan markers in figure 2(*a*) at times $n = 0, 4$ respectively in figure 4(*b,d*). While not as dramatic, at the closest approach ($n = 4$, figure 4*d*) to the UB, we also see structural resemblance. The same isosurfaces for the LB are visually indistinguishable from the initial point ($n = 0$, figure 4*a*) on the unstable manifold, and hence not shown separately in figure 4. Note that puffs are structurally (figure 4*f*) much more complicated than LB and UB.

In order to compare sizes of turbulent structures, we plotted the kinetic energy of fluctuations as a function of axial position, i.e. $k(z) = (1/2) \int_0^{D/2} \int_0^{2\pi} \boldsymbol{u} \cdot \boldsymbol{u} r \, dr \, d\theta$, for the trajectory on the unstable manifold of LB. Figure 5(*a*) shows the time interval $n \in [0, 9]$, during which the orbit leaves the neighbourhood of LB and approaches UB. During the time interval $n \in [10, 20]$ shown in figure 5(*b*), the orbit moves away from UB and becomes a puff.

5. Conclusion and outlook

In this paper, we presented strong numerical evidence that the unstable manifold of a localized relative periodic orbit of pipe flow approaches the neighbourhood of the corresponding upper-branch solution. It is remarkable that this dynamical structure in the state space persists at $Re = 1700$, which is much higher than $Re \approx 1430$, at which these orbits are born of a saddle-node bifurcation. Even though the UB is stable
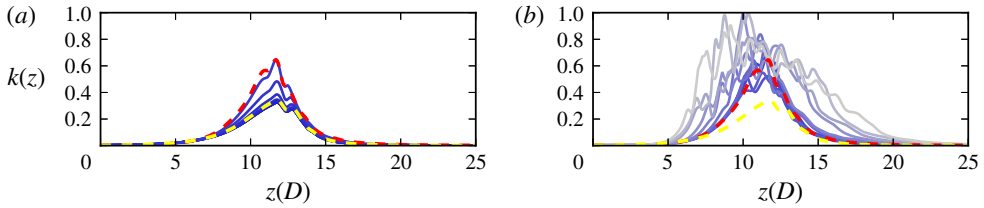
FIGURE 5. Fluctuating kinetic energy $k(z)$ contained at an axial location (z) for $n =$ 0, 1, ..., 9 (*a*) and $n =$ 10, 11, ..., 20 (*b*). THe darkest shade of blue corresponds to initial time $n = 0$, and the plotting colour becomes lighter as time increases. Dashed yellow and red curves correspond to the LB and the UB. Values of $k(z)$ are normalized by its maximum at $n = 19$.

(within the symmetry subspace) initially after the bifurcation, it quickly undergoes a series of bifurcations. At $Re = 1700$, the Arnoldi method yields seven unstable Floquet multipliers ($\Lambda > 1$) (three pairs of complex conjugates and one real), rendering its unstable manifold nine-dimensional including marginal directions. We repeated our calculation of the unstable manifold at $Re = 1900$ and obtained a qualitatively similar picture.

While the qualitative features of the unstable manifold's approach towards the UB appear to be robust, proving whether or not is there an exact connection between the unstable manifold of LB and the stable manifold of UB is a highly challenging computational task, which we did not address here. Since the sum of the dimensions of LB's unstable manifold and UB's stable manifold does not exceed the dimension of the state space, one cannot expect a generic intersection of these manifolds without fine-tuning the parameters *Re* and *L*. Our computational method is ultimately prone to the dynamical instabilities of UB, which become effective in its vicinity. Experimenting with δ values in (4.1) yielded only a marginal change in the closest distance between the unstable manifold and the UB. The numerical representation of the manifold can be improved by implementing van Veen, Kawahara & Atsushi (2011)'s formulation of the boundary value problem after symmetry reduction; however, this would be very heavy on computational resources because the problem studied here has more than two orders of magnitude more computational degrees of freedom than the ones they consider.

Previous studies (Halcrow *et al.* 2009; van Veen & Kawahara 2011) reported homoclinic and heteroclinic connections in Couette flow, which can accommodate equilibria and periodic orbits without spatial drifts. This is not the case for pressure-driven flows since all invariant solutions except the laminar equilibrium have non-zero streamwise drifts. In this regard, the current work fills an important technical gap and provides a new set of tools for study of pressure-driven flows. While the methods we used here appeared in different publications (Budanur *et al.* 2015; Ding *et al.* 2016; Budanur & Cvitanović 2017), where they are applied to much lower-dimensional systems, this is their first application to the full Navier–Stokes equations.

While Avila *et al.* (2013) show that the chaotic motion emerges from the bifurcations of the UB, as the Reynolds number is increased from 1430 to 1545, the role of the UB in transition is not obvious at $Re = 1700$. Our result shows that far from the bifurcation point, the UB takes the role of mediating the transition. Note that the UB, whose kinetic energy swings around $k = 0.5k_{HP}$, is energetically

separated from turbulent puffs, which have typical kinetic energies $k \approx 1.2 k_{HP}$. This is also clearly visible from the axial distribution of kinetic energies in figure 5 and flow structures in figure 4, where the UB clearly has a much simpler structure than puffs.

The time evolution of the spatial distribution of the kinetic energy in figure 5 suggests a two-stage transition scenario, where the spatial complexity of a puff forms as trajectories follow the unstable manifold of the UB (figure 5b). Mellibovsky *et al.* (2009) studied the transition to turbulence in a long computational domain and observed a two-stage process similar to ours at $Re = 2800$. Via 'edge tracking' (Skufca, Yorke & Eckhardt 2006) they found that a localized disturbance with chaotic dynamics resides in between the laminar and turbulent regions of the state space. When they studied the transition to turbulence from this state, they observed that the initial linear energy amplification is followed by the spread of turbulent structures accompanied by an exponential increase in the kinetic energy. Our results show that, in our symmetry-restricted setting at lower Re, this change from local amplification to spatial expansion takes place when the unstable manifold of the LB reaches the vicinity of the UB.

Ritter, Mellibovsky & Avila (2016) recently reported a detailed numerical study, where they used turbulent kinetic energy and pressure gradient as indicators to support the hypothesis that spatial complexity in this system arises as different chaotic regions in the state space merge with the neighbourhood of the UB. These observations along with ours motivate a detailed study of the UB's unstable manifold in order to understand the spatial expansion of chaotic spots. The tools we introduce here can be useful for such a study.

Acknowledgements

Appendix A. Projection operator

The projection operations (3.5) and (3.7) follow from the same geometrical principle, which we are going to derive here. Let $f^\phi(a)$ be the nonlinear semi-group action that transforms the state-space vector a according to the parameter ϕ as

$$a' = f^\phi(a), \quad \phi \in [0, \phi_{max}) \qquad (A\,1a,b)$$

and let $U(a)$ be a scalar-valued function of a that defines a codimension-1 hypersurface $U(\hat{a}) = 0$ in the state space such that at $\hat{a} = f^{\hat\phi}(a)$ a semi-group orbit of a intersects this hypersurface transversely as illustrated in figure 6. Now let us consider a small perturbation δa to a and its transformation onto this hypersurface:

$$\hat{a} + \delta\hat{a} = f^{\hat\phi + \delta\hat\phi}(a + \delta a). \qquad (A\,2)$$

Taylor-expanding the right-hand side to linear order in $\delta\hat\phi$ and δa, we obtain

$$\delta\hat{a} = \partial_\phi f^\phi(a)|_{\phi=\hat\phi} \delta\hat\phi + \left.\frac{\mathrm{d}f^\phi(a')}{\mathrm{d}a'}\right|_{a'=a} \delta a. \qquad (A\,3)$$
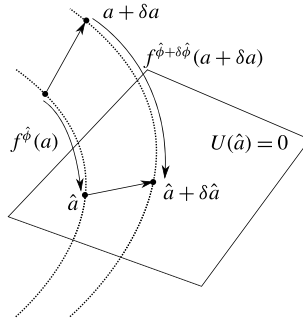
827 R1-11

FIGURE 6. Schematic illustration of the transformation of *a* and a small perturbation δa to it by the nonlinear group action $f^\phi(a)$ onto the hypersurface $U(\hat{a}) = 0$.

Our goal is to find an expression for $\delta\hat{a}$; however, (A 3) gives us one condition with two unknowns, $\delta\hat{a}$ and $\delta\hat{\phi}$. The second condition comes from the fact that (A 2) also satisfies the hypersurface equation, i.e. $U(\hat{a} + \delta\hat{a}) = 0$. Taylor expansion to the linear order yields

$$\left.\begin{array}{c} \left\langle \left.\dfrac{\mathrm{d}U(a)}{\mathrm{d}a}\right|_{a=\hat{a}}, \ \delta\hat{a} \right\rangle = 0, \\[4mm] \left\langle \left.\dfrac{\mathrm{d}U(a)}{\mathrm{d}a}\right|_{a=\hat{a}}, \ \partial_\phi f^\phi(a)|_{\phi=\hat{\phi}} \right\rangle \delta\hat{\phi} + \left\langle \left.\dfrac{\mathrm{d}U(a)}{\mathrm{d}a}\right|_{a=\hat{a}}, \ \left.\dfrac{\mathrm{d}f^\phi(a')}{\mathrm{d}a'}\right|_{a'=a} \delta a \right\rangle = 0, \end{array}\right\} \quad (\text{A}\,4)$$

where in the second step we inserted (A 3) for $\delta\hat{a}$. Solving (A 4) for $\delta\hat{\phi}$ and inserting its expression into (A 3), we find

$$\delta\hat{a} = \left.\frac{\mathrm{d}f^\phi(a')}{\mathrm{d}a'}\right|_{a'=a} \delta a - \partial_\phi f^\phi(a)|_{\phi=\hat{\phi}} \frac{\left\langle \left.\dfrac{\mathrm{d}U(a)}{\mathrm{d}a}\right|_{a=\hat{a}}, \ \left.\dfrac{\mathrm{d}f^\phi(a')}{\mathrm{d}a'}\right|_{a'=a} \delta a \right\rangle}{\left\langle \left.\dfrac{\mathrm{d}U(a)}{\mathrm{d}a}\right|_{a=\hat{a}}, \ \partial_\phi f^\phi(a)|_{\phi=\hat{\phi}} \right\rangle}, \quad (\text{A}\,5)$$

which we can rewrite as

$$\delta\hat{a} = \left(\mathbf{1} - \frac{\partial_\phi f^\phi(a)|_{\phi=\hat{\phi}} \otimes \left.\dfrac{\mathrm{d}U(a)}{\mathrm{d}a}\right|_{a=\hat{a}}}{\left\langle \left.\dfrac{\mathrm{d}U(a)}{\mathrm{d}a}\right|_{a=\hat{a}}, \ \partial_\phi f^\phi(a)|_{\phi=\hat{\phi}} \right\rangle} \right) \left.\frac{\mathrm{d}f^\phi(a')}{\mathrm{d}a'}\right|_{a'=a} \delta a, \quad (\text{A}\,6)$$

where $\otimes$ denotes the outer product. Both projection operators (3.5) and (3.7) can be obtained from (A 6) by substitutions $(l, g(l)a) \to (\phi, f^\phi(a))$ and $(\tau, f^\tau(a)) \to (\phi, f^\phi(a))$ respectively.

References

AVILA, M., MELLIBOVSKY, F., ROLAND, N. & HOF, B. 2013 Streamwise-localized solutions at the onset of turbulence in pipe flow. *Phys. Rev. Lett.* **110**, 224502.

AVILA, K., MOXEY, D., DE LOZAR, A., AVILA, M., BARKLEY, D. & HOF, B. 2011 The onset of turbulence in pipe flow. *Science* **333**, 192–196.

BUDANUR, N. B. & CVITANOVIĆ, P. 2017 Unstable manifolds of relative periodic orbits in the symmetry-reduced state space of the Kuramoto–Sivashinsky system. *J. Stat. Phys.* **167**, 636–655.

BUDANUR, N. B., CVITANOVIĆ, P., DAVIDCHACK, R. L. & SIMINOS, E. 2015 Reduction of the SO(2) symmetry for spatially extended dynamical systems. *Phys. Rev. Lett.* **114**, 084102.

CHANTRY, M., WILLIS, A. P. & KERSWELL, R. R. 2014 Genesis of streamwise-localized solutions from globally periodic traveling waves in pipe flow. *Phys. Rev. Lett.* **112**, 164501.

CHOSSAT, P. & LAUTERBACH, R. 2000 *Methods in Equivariant Bifurcations and Dynamical Systems.* World Scientific.

CVITANOVIĆ, P., ARTUSO, R., MAINIERI, R., TANNER, G. & VATTAY, G. 2015 *Chaos: Classical and Quantum.* Niels Bohr Inst.

DING, X., CHATÉ, H., CVITANOVIĆ, P., SIMINOS, E. & TAKEUCHI, K. A. 2016 Estimating the dimension of the inertial manifold from unstable periodic orbits. *Phys. Rev. Lett.* **117**, 024101.

DUGUET, Y., WILLIS, A. P. & KERSWELL, R. R. 2008 Transition in pipe flow: the saddle structure on the boundary of turbulence. *J. Fluid Mech.* **613**, 255–274.

GUCKENHEIMER, J. & HOLMES, P. 1983 *Nonlinear Oscillations, Dynamical Systems, and Bifurcations of Vector Fields.* Springer.

HALCROW, J., GIBSON, J. F., CVITANOVIĆ, P. & VISWANATH, D. 2009 Heteroclinic connections in plane Couette flow. *J. Fluid Mech.* **621**, 365–376.

HOF, B., VAN DOORNE, C. W. H., WESTERWEEL, J., NIEUWSTADT, F. T. M., FAISST, H., ECKHARDT, B., WEDIN, H., KERSWELL, R. R. & WALEFFE, F. 2004 Experimental observation of nonlinear traveling waves in turbulent pipe flow. *Science* **305**, 1594–1598.

HOPF, E. 1948 A mathematical example displaying features of turbulence. *Commun. Pure Appl. Maths* **1**, 303–322.

ITANO, T. & TOH, S. 2001 The dynamics of bursting process in wall turbulence. *J. Phys. Soc. Japan* **70**, 701–714.

JIMÉNEZ, J. & MOIN, P. 1991 The minimal flow unit in near-wall turbulence. *J. Fluid Mech.* **225**, 213–240.

KAWAHARA, G. & KIDA, S. 2001 Periodic motion embedded in plane Couette turbulence: regeneration cycle and burst. *J. Fluid Mech.* **449**, 291–300.

KAWAHARA, G., UHLMANN, M. & VAN VEEN, L. 2012 The significance of simple invariant solutions in turbulent flows. *Annu. Rev. Fluid Mech.* **44**, 203–225.

LEMOULT, G., SHI, L., AVILA, K., JALIKOP, S. V., AVILA, M. & HOF, B. 2016 Directed percolation phase transition to sustained turbulence in Couette flow. *Nat. Phys.* **12**, 254–258.

DE LOZAR, A., MELLIBOVSKY, F., AVILA, M. & HOF, B. 2012 Edge state in pipe flow experiments. *Phys. Rev. Lett.* **108**, 214502.

MELLIBOVSKY, F., MESEGUER, A., SCHNEIDER, T. M. & ECKHARDT, B. 2009 Transition in localized pipe flow turbulence. *Phys. Rev. Lett.* **103**, 054502.

PRINGLE, C. C. T. & KERSWELL, R. R. 2007 Asymmetric, helical, and mirror-symmetric traveling waves in pipe flow. *Phys. Rev. Lett.* **99**, 074502.

RITTER, P., MELLIBOVSKY, F. & AVILA, M. 2016 Emergence of spatio-temporal dynamics from exact coherent solutions in pipe flow. *New J. Phys.* **18**, 083031.

SCHNEIDER, T. M., ECKHARDT, B. & YORKE, J. 2007 Turbulence, transition, and the edge of chaos in pipe flow. *Phys. Rev. Lett.* **99**, 034502.

SKUFCA, J. D., YORKE, J. A. & ECKHARDT, B. 2006 Edge of chaos in a parallel shear flow. *Phys. Rev. Lett.* **96**, 174101.

SURI, B., TITHOF, J., GRIGORIEV, R. O. & SCHATZ, M. F. 2017 Forecasting fluid flows using the geometry of turbulence. *Phys. Rev. Lett.* **118**, 114501.

TREFETHEN, L. N. & BAU, D. 1997 *Numerical Linear Algebra.* SIAM.

VAN VEEN, L. & KAWAHARA, G. 2011 Homoclinic tangle on the edge of shear turbulence. *Phys. Rev. Lett.* **107**, 114501.

VAN VEEN, L., KAWAHARA, G. & ATSUSHI, M. 2011 On matrix-free computation of 2D unstable manifolds. *SIAM J. Sci. Comput.* **33**, 25–44.

WILLIS, A. P. 2017 The Openpipeflow Navier–Stokes solver. *SoftwareX* **6**, 124–127.

WILLIS, A. P., SHORT, K. Y. & CVITANOVIĆ, P. 2016 Symmetry reduction in high dimensions, illustrated in a turbulent pipe. *Phys. Rev. E* **93**, 022204.